Catalytic Pt-on-Au Nanostructures: Why Pt Becomes More Active on Smaller Au Particles

Gui-Rong Zhang,[†] Dan Zhao,[†] Yuan-Yuan Feng,[†] Bingsen Zhang,[‡] Dang Sheng Su,[‡] Gang Liu,[§] and Bo-Qing Xu*,[†]

[†]Innovative Catalysis Program, Key Lab of Organic Optoelectronics & Molecular Engineering, Department of Chemistry, Tsinghua University, Beijing, 100084, China, [‡]Fritz Haber Institute of the Max Planck Society, Faradayweg 4—6, d-14195 Berlin, Germany, and [§]National Center for Nanoscience and Technology, Beijing, 100190, China

ABSTRACT

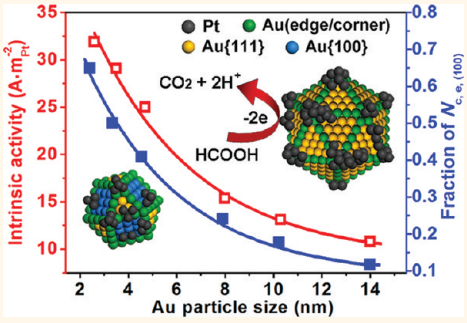

Platinum is a widely used precious metal in many catalytic nanostructures. Engineering the surface electronic structure of Pt-containing bi- or multimetallic nanostructure to enhance both the intrinsic activity and dispersion of Pt has remained a challenge. By constructing Pt-on-Au (Pt^Au) nanostructures using a series of monodisperse Au nanoparticles in the size range of 2—14 nm, we disclose herein a new approach to steadily change both properties of Pt in electrocatalysis with downsizing of the Au nanoparticles. A combined tuning of Pt dispersion and its surface electronic structure is shown as a consequence of the changes in the size and valence-band structure of Au, which leads to significantly enhanced Pt mass-activity on the small Au nanoparticles. Fully dispersed Pt entities on the smallest Au nanoparticles (2 nm) exhibit the highest mass-activity to date towards formic acid electrooxidation, being 2 orders of magnitude (75—300 folds) higher than conventional Pt/C catalyst. Fundamental relationships correlating the Pt intrinsic activity in Pt^Au nanostructures with the experimentally determined surface electronic structures (d-band center energies) of the Pt entities and their underlying Au nanoparticles are established.

KEYWORDS: gold · platinum · bimetallic nanostructure · formic acid electrooxidation · oxygen reduction · size effect · surface electronic structure

Many processes in energy conversion, chemical industry, and environmental protection depend on catalysis involving platinum (a widely used precious metal) as an indispensable component. An endeavor of intensive research in the field has been to find ways to reduce the dependence on Pt loading in the catalysts by enhancing the Pt activity with innovative Pt-containing nanostructures (*e.g.*, in polymer electrolyte membrane fuel cells[1—4] and lean-burn automobile NO_x storage-reduction technologies[5,6]). The catalytic properties of Pt-containing nanostructures are strongly dependent on their morphology (size and/or shape) and composition. The morphology effect, arising from differences in the surface electronic structure of metallic nanoparticles (NPs), can lead to dramatic increase in Pt activity for a specific reaction by selective exposure of certain Pt surface structures (*e.g.*, high-index facets like {730}, {210}, and {520}).[7,8] Unfortunately, a selective exposure of such high-activity Pt facets would require well-defined particle shapes that could be only obtained in very large sizes (*e.g.*, Pt tetrahexahedra in sizes larger than 80 nm[7]), where the majority of Pt atoms remain unexposed and unavailable for catalysis. This very inefficient use of Pt in such well-defined particles would mean an unaffordable "waste" and no hope in practical applications unless the high-activity Pt facets could be made on sufficiently small NPs.

Combining Pt with other metal element(s) to form bi- or multimetallic nanostructures could be efficient to tune the structure and catalytic activity of Pt.[3,9] Surface science studies have shown that a creation of a hetero-(metal—metal) bond in well-defined Pt surfaces may induce significant changes in the electronic structure and catalytic property of Pt.[10,11] However, the complexities of practically synthesized (realistic) Pt-containing bi- or multimetallic nanostructures often make it difficult to correlate their Pt property with those in well-defined extended surfaces of "bulk" single crystals. To date, most studies on the structure-performance correlation of Pt-containing bi- or multimetallic nanocatalysts have relied more or less on trial-and-error approaches,

* Address correspondence to bqxu@mail.tsinghua.edu.cn.

Received for review October 31, 2011 and accepted February 10, 2012.

Published online February 10, 2012
10.1021/nn204378t

in which different bi- or multimetallic nanostructure samples were obtained under widely varied conditions.[12−15] Variation in the nature of chemicals (metal precursor,[12,13] stabilizer,[14,15] reducing agent,[16] *etc.*) for the syntheses could significantly change the surface structures including particle structure (*e.g.*, twinned or single nanocrystals[17]). Among others, the particle structure of bi- or multimetallic NPs was usually unclear. How the surface geometric/electronic structure of other metals impacts the catalytic properties of Pt in "realistic" Pt-containing bi- or multimetallic catalysts remains as a fundamental issue in the field.

Recently, Pt-on-Au nanostructures based on Au NPs (denoted as Pt^Au) were shown to be viable for making good use of Pt for anodic electrocatalysis.[18−21] Pt dispersion or utilization efficiency (exposed percentage of Pt atoms or U_{Pt}) in these nanostructures may be enhanced up to 100% with proper control of Pt loading[18,19,21] and Au particle size.[15,19,21] Theoretically, Au NPs smaller than 10 nm would show enhanced electron density near the Fermi level (E_F), narrowed d-band, and higher-lying d-band center relative to bulk Au.[22−24] In addition to providing a synthetic approach to achieve full exposure of Pt atoms for catalysis, the construction of Pt^Au nanostructures would enable us to rationally tune the structure/property of Pt at nano/subnanometer scale if the size-dependent surface electronic structure of the underlying Au NPs could be adopted in experimental investigations. This concept is demonstrated here by carefully varying the Au particle size in the range of 2 to 14 nm to systematically tune the surface electronic structure of Au. For the first time, we disclose that Pt activity in these Pt^Au nanostructures correlates well with the experimentally determined surface electronic structure (d-band center energy) of Au NPs. Moreover, we demonstrate that fully dispersed Pt entities on the smallest Au NPs (2 nm) present the highest mass activity to date for anodic formic acid oxidation reaction (FAOR), being 2 orders of magnitude higher than that of Pt in conventional E-TEK Pt/C catalyst. These findings could be exploited to develop more efficient bi- or multimetallic nanostructures by design and have also broad implications for making the most efficient use of other precious metals in many electro- and/or thermal-catalytic technologies.

RESULTS AND DISCUSSION

Syntheses and Characterization of Au-*d* and Pt^Au-*d* NPs. A seed-mediated growth method was employed to synthesize a series of monodisperse Au NPs (Au-*d*) with average diameter size (*d*) ranging from 1.9 to 14.0 nm, with polyvinylpyrrolidone (PVP) as the only stabilizing agent to exclude possible interferences from using different stabilizers.[15] As illustrated in Figure 1, Pt was deposited onto the as-prepared Au-*d* particles, by reducing $PtCl_6^{2-}$ ions with hydrogen in aqueous solutions,[18,19] to prepare Pt_m^Au-*d* nanostructures (*m* denotes the atomic Pt/Au ratio). Subsequent immobilization of Pt_m^Au-*d* onto Vulcan XC-72 carbon black produced the Pt_m^Au-*d*/C samples for electrocatalysis study. Figure 2 shows the transmission electron microscopy (TEM) images and their corresponding size distribution of the as-prepared Au NPs. Their average Au diameters are *d* = 1.9, 3.2, 4.7, 8.0, 10.3, and 14.0 nm, respectively. The smallest Au-1.9 particles (Au seeds) were determined by high resolution TEM (HRTEM) and fast Fourier-transform (FFT) analysis to be 100% single crystals (SC) (Figure 2, a-2, a-3). During the subsequent growth, most of these SC particles changed to 5-fold twinned particles in icosahedron (Ih) and decahedron (Dh) shapes (Figure 2, b-2, e-2; Figure 3a). The statistics show that the particle structure of Au NPs strongly depends on their sizes (Figure 3b). The selectivity for the 5-fold twinned Ih and Dh particles was as high as 82% in Au-3.2 and increased to nearly 100% in Au-14.0 (Figure 3b). The morphology and sizes of $Pt_{0.10}$^Au-*d* particles (Supporting Information, Figure S1) were very similar to those of Au-*d* (Figure 2) except for $Pt_{0.10}$^Au-1.9, whose average diameter (2.4 nm) became 0.5 nm larger than that of Au-1.9. The immobilization of the $Pt_{0.10}$^Au-*d* particles on carbon black, however, imposed no detectable effect on the metal particle sizes (Supporting Information, Figure S1).

To estimate the coverage of Pt entities on Au NPs, we employed UV−vis spectroscopy to probe the Au surface plasmon resonance (SPR) band for Au-*d* and $Pt_{0.10}$^Au-*d* (Supporting Information, Figure S2). The SPR bands for $Pt_{0.10}$^Au-*d* were weakened significantly compared with those for their Au-*d* counterparts. As the deposited Pt entities were silent in SPR signal, these results indicate the formation of Pt-on-Au nanostructures by incomplete Pt covering of the Au NP surfaces.[15,18,19] Estimation on the number density (N_{Pt}, Table 1) of Pt atoms at the surface of Au-*d*, assuming a monatomic Pt covering of the Au surfaces, reveals that Pt atoms in every $Pt_{0.10}$^Au-*d* sample were insufficient to form a monatomic Pt-overlayer (details given in Supporting Information). Thus, the Pt deposits would present as highly dispersed two-dimensional islands or flecks at the surface of Au NPs. The decrease in N_{Pt} number with the downsizing of the underlying Au NP indicates that the dimensions or domain size of Pt in $Pt_{0.10}$^Au-*d* would decrease with the decrease in *d*, as demonstrated in our previous publications.[18,19,21] Structural information on the Pt entities was further obtained from HRTEM measurement of $Pt_{0.10}$^Au particles. A representative particle image in $Pt_{0.10}$^Au-14.0 is given in Figure 3c, which shows well-defined twinned boundaries of a multitwinned Au particle loaded with Pt entities. Note that the Pt entities appeared as single-crystallites (the lattice spacing 0.196 nm identifies Pt {200}) at the twinned boundaries of Au crystallites (the lattice spacing 0.235 and 0.202 nm

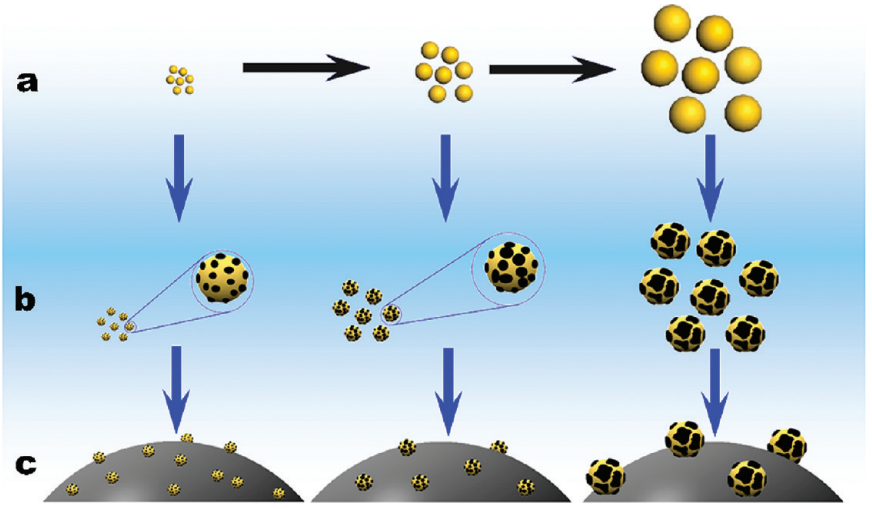

Figure 1. Schematic illustration of the syntheses of Au-*d* NPs and Pt^Au-*d* nanostructures. (a) Seed-mediated syntheses of Au NPs with varied sizes. (b) Pt^Au-*d* nanostructures prepared by reductive deposition of Pt on the preformed Au-*d* NPs. (c) Carbon immobilized Pt^Au-*d* (Pt^Au-*d* /C) nanostructures.

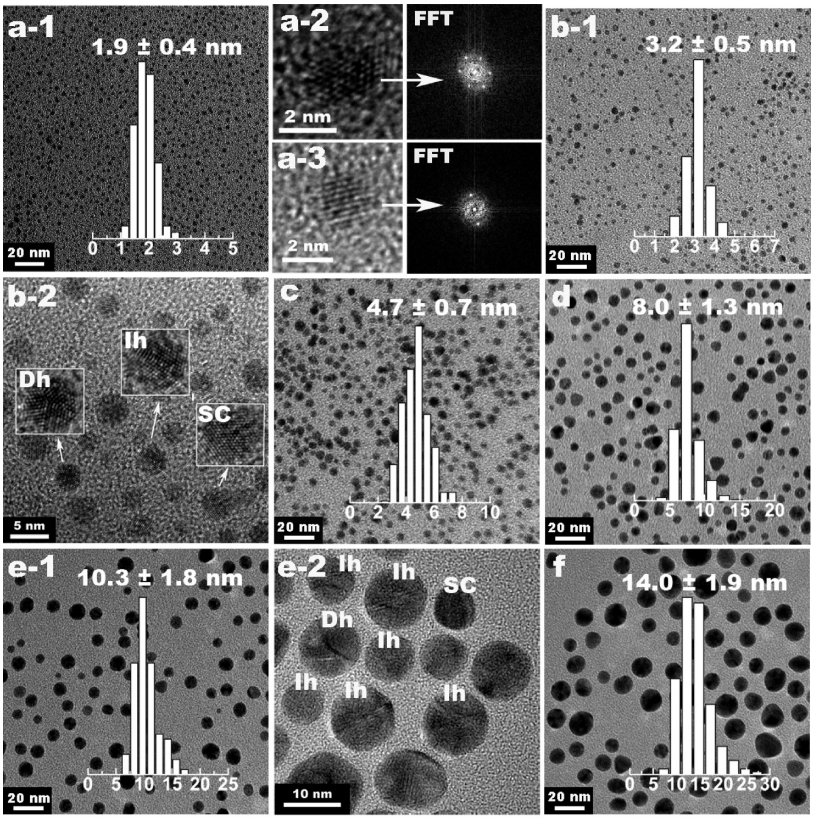

Figure 2. Representative TEM/HRTEM images and their measured size histograms of Au-*d* NPs: (a) Au-1.9, (b-1) Au-3.2, (c) Au-4.7, (d) Au-8.0, (e-1) Au-10.3, (f) Au-14.0. (a-2, a-3) HRTEM images of Au-1.9 particles and their corresponding FFT patterns. (b-2, e-2) HRTEM images for Au-3.2 and Au-10.3, respectively, showing well-defined lattice fringes of single crystal (SC), decahedron (Dh) and icosahedron (Ih) particles.

identify Au {111} and {200}, respectively). The orientation consistency of Pt {200} and Au {200} at the Pt/Au boundaries may suggest an epitaxial Pt growth on Au NPs.[25] Thus, Pt entities in the $Pt_{0.10}$^Au samples shared the same atom arrangement as the underlying Au NP surface. Since facets with higher surface energy would grow faster during growth,[26] the deposited Pt atoms would locate preferentially at the corners, edges, and {100} facets of the underlying Au NPs as illustrated schematically in Figure S3 (Supporting Information).

Figure 4 shows the cyclic voltammetry (CV) curves recorded at room temperature with a scan rate of

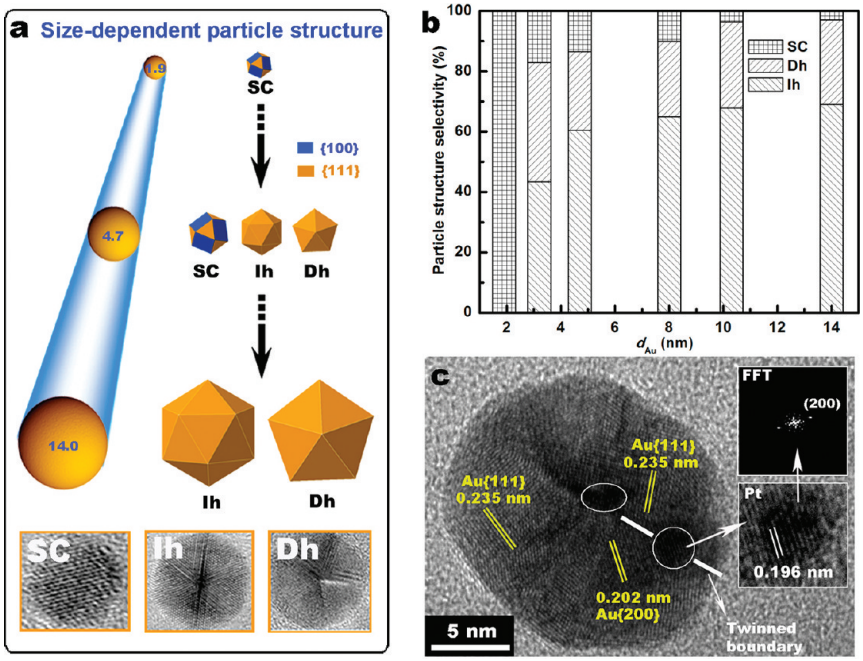

Figure 3. (a) Schematic particle structure transformation from small SC Au NPs to 5-fold twinned Ih and Dh particles during growth. (b) Particle structure selectivity for Au-*d* NPs. These data were obtained from random analyses of more than 200 particles in each sample. (c) HRTEM image of $Pt_{0.10}$^Au-14.0 showing lattice fringes for fcc Au{111} and {200} planes; the circled areas identify the presence of Pt entities. The insets show the magnified image and FFT pattern for Pt entities.

TABLE 1. Composition, Property, and Activity of Pt_m^Au Nanostructures for Anodic Formic Acid Oxidation Reaction

						catalytic activity at 0.4 V	
sample	atomic Pt/Au ratio[a]	d_{Au} (nm)[b]	N_{Pt} (nm_{Au}^{-2})[c]	EAS ($m^2 \cdot g_{Pt}^{-1}$)	U_{Pt} (%)	IA_{Pt} ($A \cdot m_{Pt}^{-2}$)	MSA_{Pt} ($A \cdot mg_{Pt}^{-1}$)
$Pt_{0.10}$^Au-14.0/C	0.10	14.0 ± 1.9	12	114	48	10.8	1.22
$Pt_{0.10}$^Au-10.3/C	0.10	10.3 ± 1.8	9	137	58	13.1	1.79
$Pt_{0.10}$^Au-8.0/C	0.10	8.0 ± 1.3	7	153	65	15.4	2.36
$Pt_{0.10}$^Au-4.7/C	0.09	4.7 ± 0.7	4	175	74	24.9	4.36
$Pt_{0.15}$^Au-3.2/C	0.15	3.2 ± 0.5	4	189	80	26.6	5.03
$Pt_{0.10}$^Au-3.2/C	0.09	3.2 ± 0.5	3	210	89	28.1	5.85
$Pt_{0.20}$^Au-1.9/C	0.20	1.9 ± 0.4	4	178	76	29.5	5.31
$Pt_{0.10}$^Au-1.9/C	0.10	1.9 ± 0.4	2	233	99	31.9	7.50
Pt/C (E-TEK)				77	33	1.3	0.10

[a] Atomic Pt/Au ratio was determined by ICP—AES. [b] Average Au particle size in diameter, more than 300 particles were randomly taken in different TEM images for measuring the sizes and their distribution. [c] Number of Pt atoms per square nanometer of Au surface (number density, see Supporting Information for detail)..

20 $mV \cdot s^{-1}$ on $Pt_{0.10}$^Au-*d*/C samples in 0.5 M H_2SO_4 solution. These CV curves show the redox signals associated with the chemistry of H adsorption—desorption ($H^+ + e^- \leftrightarrow H_{ad}$) on Pt in the potential region of −0.24 to 0 V. The prominent positive peaks at *ca.* −0.2 V feature the H desorption from highly coordinatively unsaturated Pt sites.[18,19] It is seen that the H desorption peak potential for $Pt_{0.10}$^Au-*d*/C shifted toward lower potentials on increasing the Au size *d*, which is especially apparent when comparing the peaks for the samples of $d > 4.7$ nm. Specifically, the H desorption peak potential was −0.190 V for $Pt_{0.10}$^Au-1.9/C, −0.193 V for $Pt_{0.10}$^Au-4.7/C, and −0.223 V for $Pt_{0.10}$^Au-14.0/C. These data indicate that Pt sites on smaller Au NPs have a stronger bonding for adsorbed H since a higher H desorption peak potential would mean a stronger bonding of H at the Pt sites. Therefore, Pt sites in $Pt_{0.10}$^Au-*d* of smaller *d* are in more coordinatively unsaturated states.[18,19]

The intensity of the H desorption peak in Figure 4, which decreased with the increase in *d* for the $Pt_{0.10}$^Au-*d*/C samples, characterizes the number of adsorbed H atoms on surface Pt sites. The numbers of adsorbed H atoms measured from Figure 4 are then used to obtain the electrochemically active surface area (EAS) data of Pt in the $Pt_{0.10}$^Au-*d* nanostructures (see Supporting Information for the detail). Table 1 presents the Pt EAS data measured as such and their derived utilization efficiency of Pt (U_{Pt})[18,19] for the $Pt_{0.10}$^Au-*d* nanostructures. Pt entities in these samples

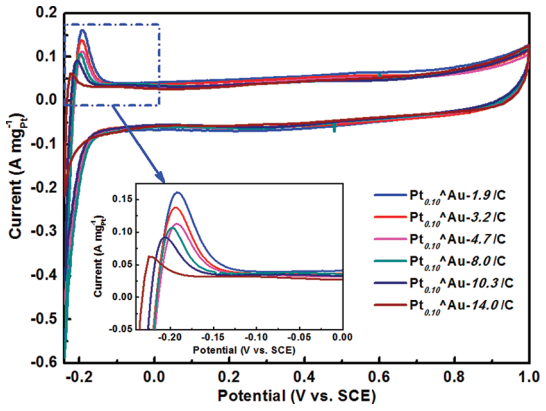

Figure 4. Cyclic voltammetry curves of $Pt_{0.10}$^Au-*d*/C nanostructures in 0.5 M H_2SO_4 at a scan rate of 20 mV s^{-1}.

appear highly dispersed (U_{Pt} > 45%), but the downsizing of the Au NP leads to dramatic enhancement in EAS and U_{Pt}. In other words, the dimension of Pt entities in $Pt_{0.10}$^Au-*d* decreases with the size of Au NP (Supporting Information, Figure S4).[15,18,19] For instance, the EAS and U_{Pt} values for $Pt_{0.10}$^Au-*d* were enhanced from 114 $m^2 \cdot g_{Pt}^{-1}$ and 48% at *d* = 14.0 nm to 153 $m^2 \cdot g_{Pt}^{-1}$ and 65% at *d* = 8.0 nm, and then 233 $m^2 \cdot g_{Pt}^{-1}$ and 99% at *d* = 1.9 nm. Note that with the specific atomic Pt/Au ratio (*m* = 0.10), a complete exposure of all Pt atoms for catalysis ($U_{Pt} \approx$ 100%) could not be reached unless the Au size was reduced to *ca*. 1.9 nm. Therefore, the smaller Au NPs allow to expose all Pt atoms for catalysis at higher Pt loadings in the Pt^Au nanostructures, which may be important in technologies where a high density of catalytic sites is necessary (*e.g.*, high power density electrodes[2]).

Catalytic Properties of Pt^Au-*d* Nanostructures for FAOR. Figure 5a compares the anodic-scan CV curves of FAOR for $Pt_{0.10}$^Au-*d*/C, Au-1.9/C, and conventional Pt/C (E-TEK) catalysts (complete CV curves are shown in the Supporting Information, Figure S5). The curve for Au-1.9/C (without Pt) showed no oxidation current, but two current peaks at around 0.40 and 0.80 V were detected on Pt/C catalyst. It is well accepted that FAOR on Pt would follow the so-called "dual pathways" mechanism.[27−29] One is a direct pathway involving a fast oxidation of HCOOH to CO_2 *via* very active intermediates (*e.g.*, $HCOO_{ad}$), which is evidenced from the oxidation currents recorded below the onset potential of OH_{ad} formation on the Pt surface (0.6 V). The other is an indirect pathway involving at least one poisonous intermediate identified mainly as CO_{ad} from the dehydration of HCOOH; a further oxidation of the intermediate to CO_2 would require a potential higher than 0.6 V.[28,29] Accordingly, the current peak at around 0.40 V would be associated with the oxidation of HCOOH to form CO_2 in the direct reaction pathway while the other peak at around 0.80 V may be related with the formation of adsorbed CO-like intermediate by the indirect reaction pathway, as documented in earlier literature.[28,29] In contrast, all of the $Pt_{0.10}$^Au-*d*/C catalysts showed only one distinct peak at potentials lower than 0.6 V, indicating that FAOR proceeds predominantly *via* the direct reaction pathway over the highly dispersed Pt entities carried by Au NPs.[15,20,21,30]

The current of FAOR in Figure 5a increases with the downsizing of the Au NP in the $Pt_{0.10}$^Au nanostructures. The intrinsic activity (IA_{Pt}) and mass-specific activity (MSA_{Pt}) data in Table 1 quantitatively show the calibrated Pt activity at 0.40 V. These activity data strongly correlate with the size of the underlying Au NP, that is, Pt entities deposited on smaller Au NP always showed a higher activity. On the basis of IA_{Pt} data, $Pt_{0.10}$^Au-1.9/C (31.9 $A \cdot m_{Pt}^{-2}$) is 3 times more active than $Pt_{0.10}$^Au-14.0/C (10.8 $A \cdot m_{Pt}^{-2}$) and 25 times more active than conventional Pt/C (1.3 $A \cdot m_{Pt}^{-2}$) catalyst. As Pt entities on smaller Au NPs had better exposure (higher U_{Pt}), the enhancement in MSA_{Pt} became much more significant, making $Pt_{0.10}$^Au-1.9/C (7.50 $A \cdot mg_{Pt}^{-1}$) 6 and 75 times more active than $Pt_{0.10}$^Au-14.0/C (1.22 $A \cdot mg_{Pt}^{-1}$) and Pt/C (0.10 $A \cdot mg_{Pt}^{-1}$), respectively.

The above discussion takes no consideration of a possibility that the decreased activity of Pt in $Pt_{0.10}$^Au-*d* samples of *d* ≥ 3.2 nm might be induced by the presence of ascorbic acid (AA) or its oxidized species since the high-activity sample $Pt_{0.10}$^Au-1.9 was prepared from the smallest Au NPs (Au-1.9) that were synthesized without the use of AA. To make it clear, a $Pt_{0.10}$^Au-1.9-AA/C catalyst was prepared by Pt deposition on AA-treated Au seeds (Au-1.9-AA). As detailed in the Supporting Information, this Au-1.9-AA sample was prepared at room temperature by continued stirring for 24 h of an as-prepared solution of the colloidal Au seeds with the presence of AA (molar AA/Au = 1.5). The electrocatalytic performance in FAOR of this $Pt_{0.10}$^Au-1.9-AA/C catalyst was found very similar to that of $Pt_{0.10}$^Au-1.9/C without the treatment with AA (Figure S6 in Supporting Information). The EAS and MSA_{Pt} (at 0.4 V) for $Pt_{0.10}$^Au-1.9-AA/C were 228 $m^2 \cdot g_{Pt}^{-1}$ and 7.6 $A \cdot mg_{Pt}^{-1}$, respectively, which cannot be discriminated from those for $Pt_{0.10}$^Au-1.9/C (233 $m^2 \cdot g_{Pt}^{-1}$ and 7.5 $A \cdot mg_{Pt}^{-1}$). These data indicate that the presence of AA and possibly its derivates has little effect on the catalytic activity of our Pt^Au nanostructures.

The variation in IA_{Pt} (Table 1) demonstrates the structure-sensitive nature of FAOR on Pt. The downsizing of the Au NP from 14 to 2 nm resulted in continued IA_{Pt} enhancement as plotted in Figure 5b. To separate the effect of U_{Pt} (or Pt dispersion) from that of Au size, we increased the Pt loading on Au-1.9 and Au-3.2 to *m* = 0.20 and 0.15, respectively, attempting to prepare several Pt^Au samples of different Au sizes but similar U_{Pt}. The U_{Pt} data of the resultant $Pt_{0.20}$^Au-1.9/C (76%) and $Pt_{0.15}$^Au-3.2/C (80%) were found similar to that of $Pt_{0.10}$^Au-4.7/C (74%), as seen in Table 1. The IA_{Pt} order of these three samples was, however, $Pt_{0.20}$^Au-1.9/C

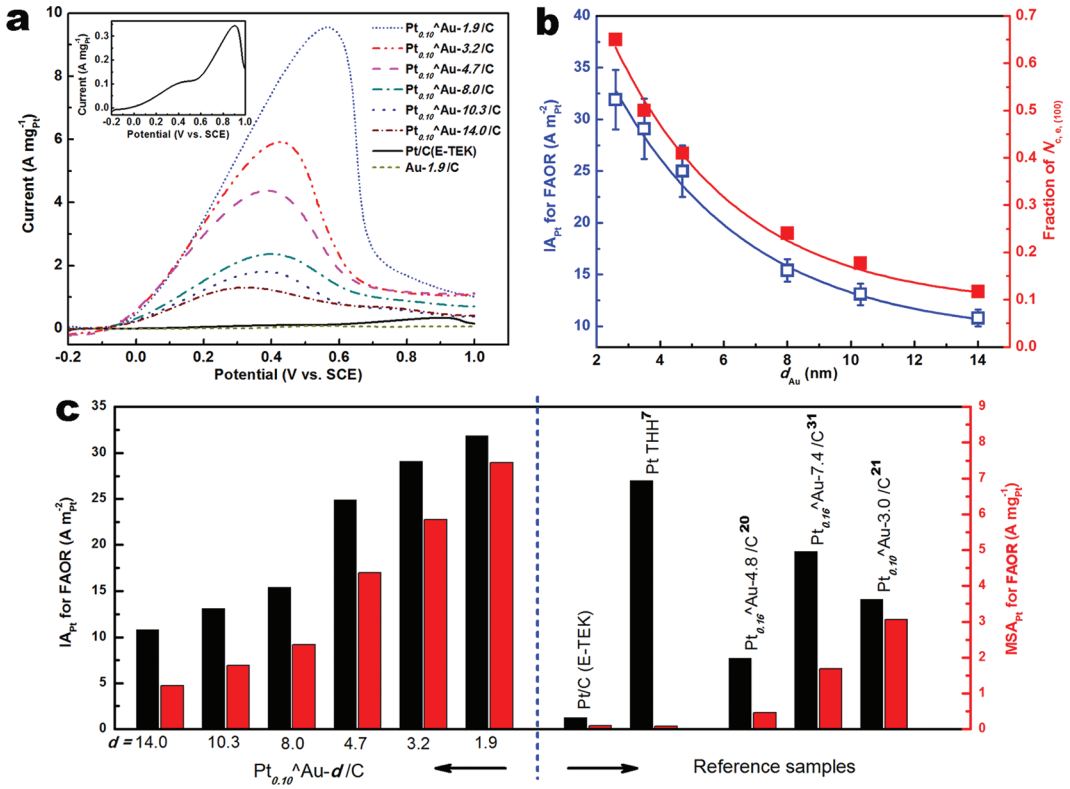

Figure 5. (a) Anodic-scan CV curves for FAOR on $Pt_{0.10}$^Au-*d*/C, Pt/C (E-TEK), and Au-1.9/C. The inset shows the magnified curve on Pt/C (E-TEK). (b) Dependences of IA_{Pt} toward FAOR of the $Pt_{0.10}$^Au-*d* nanostructures (blue) and fraction of Au surface atoms at corners, edges and (100) facets (red) on the particle size of Au. (c) Comparison of the Pt activity data for FAOR (at 0.40 V) in $Pt_{0.10}$^Au-*d*/C with those of high-activity nanostructures in literature.

(30 $A \cdot m_{Pt}^{-2}$) > $Pt_{0.15}$^Au-3.2/C (27 $A \cdot m_{Pt}^{-2}$) > $Pt_{0.10}$^Au-4.7/C (25 $A \cdot m_{Pt}^{-2}$). Indeed, the Au particle size significantly impacts the Pt activity in Pt_m^Au-*d* nanostructures. This is the first time to clearly show the Au size-effect on Pt activity in Pt-on-Au nanostructures, in which systematically sized Au NPs were capped with the same stabilizer (PVP), and the Pt dispersion was kept almost unchanged.

To understand how Pt activity gets improved with downsizing Au NP in $Pt_{0.10}$^Au-*d*, we try to correlate the Pt activity with the population of specific surface Au sites. Analysis of the particle structure of Au NPs by HRTEM (Figure 2) enabled us to further estimate the fraction of surface Au atoms at different locations (corners, edges, and (111) and (100) facets, Figure S7 in Supporting Information), according to the particle structure selectivity of Au NPs (Figure 3b). As the difference of atoms at different locations stems essentially from their varied coordination numbers (CNs), we discriminate the Au surface atoms in two classes according to their CNs: (i) low energy surface atoms of CN = 9 at the (111) facets, $N_{(111)}$; (ii) high energy surface atoms at the corners (CN = 6), edges (CN = 7), and (100) facets (CN = 8), $N_{c,e,(100)}$. The fraction of $N_{c,e,(100)}$ at the Au surface is plotted against d_{Au} in Figure 5b using the right vertical axis. Evidently, this fraction of high energy surface atoms varies almost in parallel with IA_{Pt} on downsizing the Au NP. Therefore, it can be concluded that the surface energy state of Au NPs determines the catalytic activity of their carrying Pt entities.

Figure 5c clearly shows, based on comparison of IA_{Pt} and MSA_{Pt} data, that the present $Pt_{0.10}$^Au-*d* catalysts of *d* < *ca.* 5 nm are superior to those of the representative high-activity Pt catalysts documented in literature.[7,20,21,31] $Pt_{0.10}$^Au-1.9/C appears to be the most active catalyst by both IA_{Pt} and MSA_{Pt}. Those tetrahexahedral (THH) Pt NPs enclosed with high-index {730}, {210}, and {520} facets[7] showed a high IA_{Pt} (ca. 28 $A \cdot m_{Pt}^{-2}$) close to that of $Pt_{0.10}$^Au-1.9 (32 $A \cdot m_{Pt}^{-2}$). But, the very large sizes (>80 nm) of the THH Pt NPs make their MSA_{Pt} (0.08 $A \cdot mg_{Pt}^{-1}$) 2 orders of magnitude lower, even lower than conventional Pt/C (0.10 $A \cdot mg_{Pt}^{-1}$) catalyst. A high activity by Pt mass is essential for practical applications as the precious metal is priced by mass (weight), rather than by surface area. Thus, the MSA_{Pt} number could be recommended to characterize the gain/cost factor of Pt-based catalysts.[18,21] Other Pt-on-Au nanostructures, which were obtained by Pt deposition on citrate-stabilized (4.8 nm),[20] PVA-stabilized (3.0 nm),[21,32] or oleylamine-stabilized (7.4 nm)[31] Au NPs, showed much lower IA_{Pt}. We can therefore conclude that the $Pt_{0.10}$^Au-1.9 catalyst presents to date the highest MSA_{Pt} for FAOR.

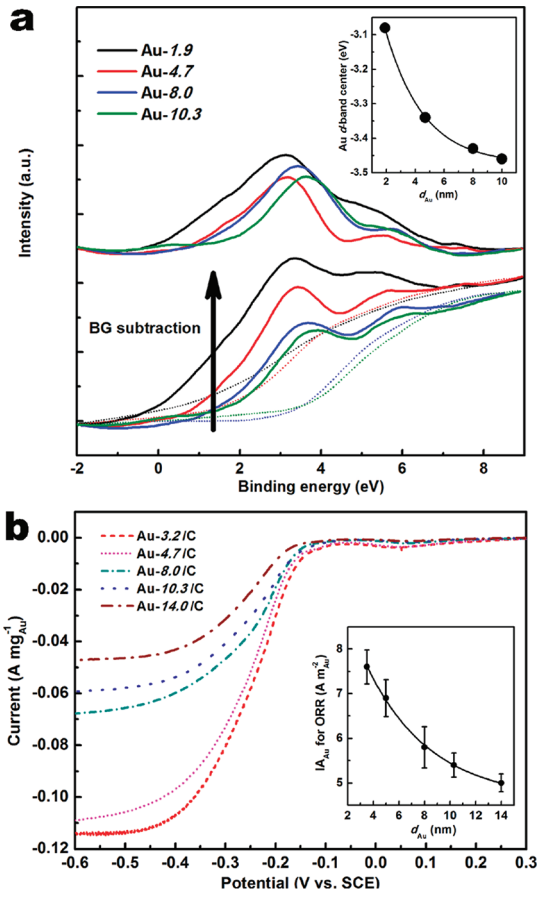

Figure 6. (a) As-measured and background-subtracted (upper) valence-band XPS spectra of Au-*d* NPs. The Shirley backgrounds are shown as the dotted curves. The inset shows the d-band center energies as a function of the Au particle size. (b) Polarization curves of ORR on Au-*d*/C. The inset correlates IA_{Au} (at −0.25 V) with the Au particle size.

When the total mass of Pt and Au is taken into account, the $MSA_{metal(Pt+Au)}$ of $Pt_{0.10}$^Au-1.9 is still 6.8 times higher than the MSA_{Pt} of conventional Pt/C, and 8.5 times higher than that of the THH-Pt catalyst.[7] In this regard, the $Pt_{0.10}$^Au-1.9 could reduce the cost of Pt catalyst by a factor of 7−15 while holding an equivalent performance to the conventional Pt/C catalyst for FAOR.

Physical and Chemical Properties of Au-*d* and $Pt_{0.10}$^Au-*d* NPs. Before discussing the surface electronic properties of $Pt_{0.10}$^Au-*d*, it is important to explore the size-dependent valence-band properties of Au NPs. It is known that the metal valence-band structure, usually described quantitatively in terms of the d-band center energy, can be significantly affected by the surface structure or coordination number of surface atoms.[33,34] We use valence-band X-ray photoelectron spectroscopy (XPS) to measure the valence-band structure of Au-*d* samples (Figure 6a). After subtraction of the Shirley backgrounds, the intensity signals of the valence-band spectra are proportional to the density of states (DOS).[35] Clearly, the DOS (intensity) near E_F and valence-bandwidth increased steadily with downsizing the Au NP. The inset of Figure 6a quantitatively shows the relationship between the surface electronic structure by d-band center (energy from E_F) and the size of Au NPs (d_{Au}). The valence d-band center is lowered with decreasing d_{Au}, from −3.1 eV for Au-1.9 to −3.3 eV for Au-4.7, and −3.5 eV for Au-10.3. These numbers agree well with those obtained in theoretical calculations,[24] namely −3.1, −3.3, and −3.4 eV, respectively, for 2, 5, and 10 nm Au NPs. Thus, the results in Figure 6a provide the first experimental verification for the theory that smaller Au NPs would have higher d-band center energies.[24] The variation in valence-band structure of Au NP could modify the electronic and catalytic properties of its carrying Pt, as shown in theoretical and experimental studies of supported metal clusters on Au (111)[36] and single crystal transition metal surfaces.[37]

How the d-band center would affect the property of Au NPs in electrocatalysis is still an open question. As Pt with a relatively lower d-band center would have a higher activity for oxygen reduction reaction (ORR),[37−39] we employed the cathode ORR to probe the d-band center effect on the catalytic property of Au-*d* particles after they were immobilized on carbon black. TEM analysis confirmed that the Au particle sizes were kept unchanged on the carbon support except for Au-1.9, whose average size increased to 5.1 nm after the immobilization (Supporting Information, Figure S8). Figure 6b reports the polarization curves of ORR in O_2-saturated 0.5 M KOH electrolyte, showing the currents normalized to the Au loading. The kinetic currents derived from these polarization curves are then normalized after mass-transport correction to the electrochemically active surface area of Au (EAS_{Au}, obtained by using the method of Trasatti and Petrii[40]) to quantitatively compare the intrinsic activity (IA_{Au}) of Au-*d*, as shown in the inset of Figure 6b. These data clearly show that Au NPs with higher d-band center energies would be more active toward ORR. Another translation of these data leads to the establishment of a good correlation between the IA_{Au} and the fraction of $N_{c,e,(100)}$ at the surface of Au-*d* particles (Supporting Information, Figure S9) since the Au d-band center and the fraction of $N_{c,e,(100)}$ are actually closely related. All these correlations point to that the size-dependent catalytic property of Au NPs is closely associated with the variation in the coordination state of surface Au atoms. This would not be surprising since it is well established that ORR on single crystal Au(*hkl*) is very structure-sensitive in an alkaline electrolyte, showing the activity order (IA_{Au}) of Au(111) < Au(110) < Au(100).[41,42]

ORR was also conducted on $Pt_{0.10}$^Au-*d*/C catalysts to study whether the Pt d-band center could be affected by the size of Au NP. The results (Figure 7a) show that Pt entities on smaller Au NPs are inferior to those on larger Au NPs. The IA_{Pt} data, which were obtained by

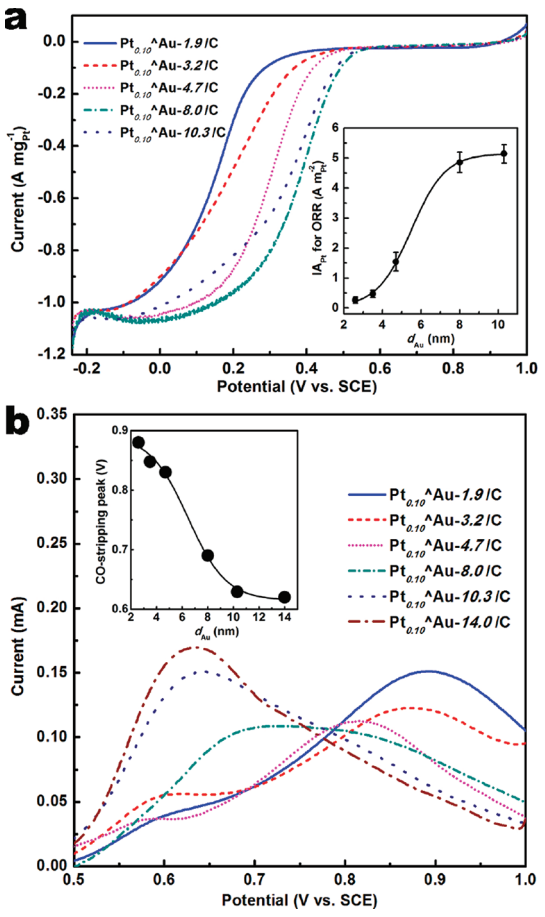

Figure 7. (a) Polarization curves of ORR on $Pt_{0.10}$^Au-*d*/C. The inset correlates IA_{Pt} (at 0.35 V) with the Au particle size. (b) Backgound-subtracted anodic-scan CO-stripping curves on $Pt_{0.10}$^Au-*d*/C. The inset correlates the CO-stripping peak potential with the Au particle size.

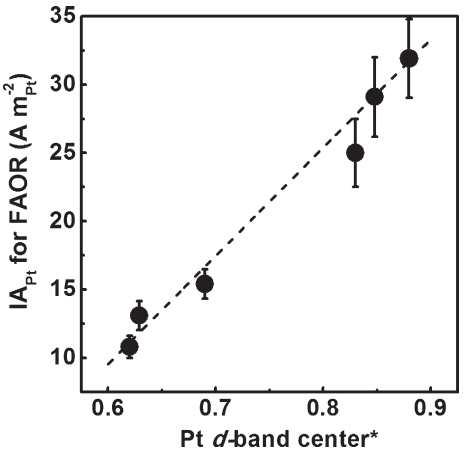

Figure 8. Correlation between the IA_{Pt} for FAOR and the "Pt d-band center*" as scaled by the CO-stripping peak potentials for $Pt_{0.10}$^Au-*d* catalysts.

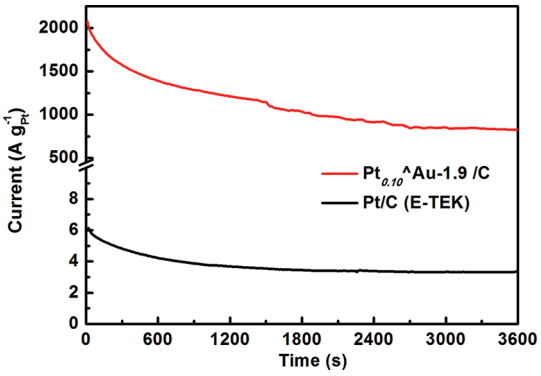

Figure 9. Long-term catalytic activity and stability of $Pt_{0.10}$^Au-1.9/C for FAOR in comparison with conventional Pt/C (E-TEK) catalyst.

normalizing the kinetic current to the EAS of Pt in $Pt_{0.10}$^Au-*d*/C, increased monotonously with increasing d_{Au}, as shown in the inset of Figure 7a. The difference in IA_{Pt} was as high as 20 times between $Pt_{0.10}$^Au-10.3/C and $Pt_{0.10}$^Au-1.9/C. These IA_{Pt} data demonstrate that downsizing the Au NP up-shifted the d-band center of their carried Pt entities. Thus, Pt entities having higher d-band center energies would have stronger bonding with their adsorbed O and OH species and then produce slower overall ORR kinetics.

The relative d-band center energies of Pt in the $Pt_{0.10}$^Au-*d* nanostructures were double checked with the independent data from electrochemical CO-stripping studies, as the CO-stripping peak potential on Pt catalysts correlates directly with the Pt d-band center.[33,43,44] A higher lying Pt d-band center can lead to a stronger CO adsorption due to a decreased electron back-donation from Pt to the antibonding orbitals of CO molecules.[43] Figure 7b shows the background-subtracted CO-stripping curves on the $Pt_{0.10}$^Au-*d* nanostructures. Indeed, the CO-stripping peak position on $Pt_{0.10}$^Au-*d* shifted steadily to higher potentials with downsizing of the Au NP. The small shoulder peaks at *ca.* 0.6 V would arise from the oxidation of CO adsorbed on the uncovered Pt-free Au surface of the $Pt_{0.10}$^Au-*d* samples, which was documented in earlier literature.[45,46] Thus, the present Pt-related CO-stripping peak potential data are a further piece of strong evidence that Pt entities on smaller Au NPs have a higher d-band center than those on larger Au NPs.

Both the IA_{Pt} for ORR (Figure 7a) and CO-stripping peak potential (Figure 7b) indicate that the Pt d-band center in $Pt_{0.10}$^Au-*d* shifts up with downsizing Au NP. These results would imply that the high-energy surface Au atoms up-tuning the d-band center of Au NP also enhance the d-band center of the Pt entities in $Pt_{0.10}$^Au-*d*, probably due to valence-band coupling.[10,36] Density functional theory (DFT) calculations have disclosed that the d-band center energy for Pt overlayer (−1.80 eV) on Au surface is significantly higher than that for bulk Pt (−2.25 eV).[47] This up-shifted d-band center happens to equal that of

Pd (−1.80 eV), on which anodic FAOR proceeds exclusively *via* the direct reaction pathway.[48] Figure 8 correlates the IA_{Pt} for FAOR of $Pt_{0.10}$^Au-*d* with the "Pt d-band center*" scaled by the CO-stripping peak potential (Figure 7b), which indicates that Pt entities having higher Pt d-band center energies are intrinsically more active in having FAOR proceeded on the direct reaction pathway. These data uncover the nature behind the activity change of Pt entities for FAOR in the $Pt_{0.10}$^Au-*d* nanostructures. This correlation could have important implications for establishing a physical basis to anticipate the Pt activity in different nanostructures.

Moreover, chronoamperometric (CA) measurements of FAOR were carried out to compare the long-term catalytic activity and stability of $Pt_{0.10}$^Au-1.9/C with conventional Pt/C catalyst (Figure 9). The current density was recorded at a practical operating voltage (0.06 V)[49] for 60 min. Surprisingly, the steady state Pt mass activity of $Pt_{0.10}$^Au-1.9/C (823 $A \cdot g_{Pt}^{-1}$) remained ~300 times higher than that of Pt/C catalyst (3 $A \cdot g_{Pt}^{-1}$), demonstrating the great advantage of Pt_m^Au-*d* nanostructures for Pt-saving catalytic electrodes.

CONCLUSIONS

This work points out for the first time two important correlations for Pt-on-Au nanostructures in electrocatalysis: one correlates the Pt activity for FAOR with the surface electronic structure of Pt, and the other correlates the surface electronic structures of Pt and their underlying Au NPs. These findings provide unprecedented insights into the fundamental interactions and effects that control the activity of Pt.

The surprisingly high activity of Pt in the $Pt_{0.10}$^Au-1.9 catalyst for FAOR demonstrates a new avenue to high-efficiency Pt catalyst, namely to construct Pt entities with desirable surface electronic structures in bi- or multimetallic nanostructures by engineering at the nanoscale the valence-band structure of the underlying metal NPs, which may be exploited to develop new and high-performing metallic nanostructures for saving precious metals in catalysts used for other technological applications.

METHODS

Synthesis. A stepwise seed-mediated growth approach was employed to synthesize monodisperse Au NPs in diameters of 3.2−14.0 nm using polyvinylpyrrolidone (PVP) and ascorbic acid as the stabilizer and reductant, respectively. The starting Au seeds were in diameters of 1.9 nm and were obtained by reduction of aqueous $HAuCl_4$ with $NaBH_4$ in the presence of PVP. Pt_m^Au-*d* nanostructures were prepared by reducing $PtCl_6^{2-}$ onto as-prepared Au-*d* NPs using hydrogen as the reductant according to the procedure described previously.[18,19] Detailed preparation procedures can be found in the Supporting Information.

Structural Analysis. TEM images were taken using a JEOL JEM-2010 microscope operated at 120 kV. High-resolution TEM images were obtained on a Philips CM200 FEG or FEI Tecnai G^2 F20 U-TWIN microscope (both at 200 kV accelerating voltage). The samples were prepared by placing a drop of the colloidal solution or catalyst powder dispersion in deionized water on a Formvar/carbon film coated Cu grid (3 mm, 300 mesh), followed by drying under ambient conditions.

UV−vis spectroscopy was recorded on a Unico UV-2102PC spectrometer operated at a resolution of 0.5 nm. The colloidal solution samples were filled in a quartz cell of 1 cm light-path length, and the light absorption spectra were given in reference to deionized water.

High resolution valence band XPS measurements were carried out on an ESCALAB250 (VG Thermo) high performance electron spectrometer equipped with monochromated Al Kα X-ray radiation (1484.6 eV). The analyzer was in the constant analyzer energy (CAE) mode at a pass energy of 30 eV for all the valence band XPS measurements. The binding energies were measured with an accuracy of ±0.1 eV, and were given with respect to the Au Fermi edge (E_F), assuming that the E_F is at 0 eV. The as-measured valence band XPS spectra, shown in Figure 6a, were smoothed to reduce noises by using Origin 8.0 software (Origin-Lab Corporation, Northampton, MA). For the accurate comparison of all valence band XPS spectra, the secondary electron background (Shirley-type, which is fitted by using a XPS Peak 4.1 software) was subtracted from the measured spectra. The upper limit of the binding energy was fixed at 9.0 eV for every valence-band XPS spectrum during the integration. The position of the d-band center is given by $\int N(\varepsilon)\varepsilon\, d\varepsilon / \int N(\varepsilon)\, d\varepsilon$, where $N(\varepsilon)$ is the density of state (*i.e.*, the photoelectron intensity after background subtraction).

The actual loading amount and composition of Pt and Au in the as-prepared carbon-supported catalysts were determined by ICP−AES (IRIS Intrepid II XSP, ThermoFisher), and the loading of Au was determined to be around 5 wt % in all the investigated Au-*d*/C and $Pt_{0.10}$^Au /C samples.

Electrochemical Characterization. Electrochemical measurements were performed on a potentiostat/galvanostat model 263A (PAR) controlled by PowerSuite software. A saturated calomel electrode (SCE) and a Pt wire (diameter = 0.5 mm) were used as reference electrode and counter-electrode, respectively. All potentials reported in this work are given with respect to SCE. HCOOH electrooxidation reaction was studied by recording CV curves at a scanning rate of 20 $mV \cdot s^{-1}$ from −0.2 to 1.0 V in 0.5 M H_2SO_4 with 2.0 M HCOOH. Chronoamperometric (CA) measurements of FAOR were carried out under continuous operating conditions. The current density was recorded at a practical operating voltage of 0.06 V for 60 min. The ORR measurements were performed in O_2-saturated 0.5 M KOH (Au-*d*/C) or 0.5 M H_2SO_4 ($Pt_{0.10}$^Au-*d*/C) electrolyte using a glassy carbon rotating disk electrode (PINE) at a rotation rate of 1600 rpm, and the polarization curves were recorded at a scanning rate of 10 $mV \cdot s^{-1}$. At least four electrochemical experimental data sets were collected to generate the error bars, which were defined as the standard deviations of specific current.

Conflict of Interest: The authors declare no competing financial interest.

Acknowledgment. We thank Drs. W. X. Huang and Z. Q. Jiang (Department of Chemical Physics, University of Science and Technology of China) for their kind help and discussion on experimentation and measurement of high resolution valence-band XPS. We also thank Professor J. C. Védrine (Université P.&M. Curie-Paris VI, France) for his help in English on the occasion of his visit to our laboratory. This work was financially supported by NSF (Grants 21033004 and 20921001) of China.

Supporting Information Available: Information about experimental protocols, estimation of the surface structure of Au

nanoparticles, determination of the active surface area and utilization of Pt; extended TEM images and electrochemical characterization data of the nanostructures. This material is available free of charge *via* the Internet at http://pubs.acs.org.

REFERENCES AND NOTES

1. Steele, B. C. H.; Heinzel, A. Materials for Fuel-Cell Technologies. *Nature* **2001**, *414*, 345–352.
2. Gasteiger, H. A.; Kocha, S. S.; Sompalli, B.; Wagner, F. T. Activity Benchmarks and Requirements for Pt, Pt-Alloy, and Non-Pt Oxygen Reduction Catalysts for PEMFCs. *Appl. Catal., B* **2005**, *56*, 9–35.
3. Stamenkovic, V. R.; Fowler, B.; Mun, B. S.; Wang, G. F.; Ross, P. N.; Lucas, C. A.; Markovic, N. M. Improved Oxygen Reduction Activities on $Pt_3Ni(111)$ *via* Increased Surface Site Availability. *Science* **2007**, *315*, 493–497.
4. Yamamoto, K.; Imaoka, T.; Chun, W. J.; Enoki, O.; Katoh, H.; Takenaga, M.; Sonoi, A. Size-Specific Catalytic Activity of Platinum Clusters Enhances Oxygen Reduction Reactions. *Nat. Chem.* **2009**, *1*, 397–402.
5. Parks, J. E. Less Costly Catalysts for Controlling Engine Emissions. *Science* **2010**, *327*, 1584–1585.
6. Granger, P.; Parvulescu, V. I. Catalytic NO_x Abatement Systems for Mobile Sources: From Three-Way to Lean Burn After-Treatment Technologies. *Chem. Rev.* **2011**, *111*, 3155–3207.
7. Tian, N.; Zhou, Z.; Sun, S.; Ding, Y.; Wang, Z. L. Synthesis of Tetrahexahedral Platinum Nanocrystals with High-Index Facets and High Electro-oxidation Activity. *Science* **2007**, *316*, 732–735.
8. Narayanan, R.; El-Sayed, M. A. Changing Catalytic Activity During Colloidal Platinum Nanocatalysis Due to Shape Changes: Electron-Transfer Reaction. *J. Am. Chem. Soc.* **2004**, *126*, 7194–7195.
9. Gasteiger, H. A.; Markovic, N.; Ross, P. N.; Cairns, E. J. Methanol Electrooxidation On Well-Characterized Platinum−Ruthenium Bulk Alloys. *J. Phys. Chem.* **1993**, *97*, 12020–12029.
10. Rodriguez, J. A.; Goodman, D. W. The Nature of the Metal Metal Bond in Bimetallic Surfaces. *Science* **1992**, *257*, 897–903.
11. Ruckman, M. W.; Strongin, M. Monolayer Metal-Films on Metallic Surfaces—Correlation between Electronic-Structure and Molecular Chemisorption. *Acc. Chem. Res.* **1994**, *27*, 250–256.
12. Zhao, D.; Yan, B.; Xu, B. Q. Proper Alloying of Pt with Underlying Ag Nanoparticles Leads to Dramatic Activity Enhancement of Pt Electrocatalyst. *Electrochem. Commun.* **2008**, *10*, 884–887.
13. Zhao, D.; Wang, Y. H.; Yan, B.; Xu, B. Q. Manipulation of Pt^Au Nanostructures for Advanced Electrocatalyst. *J. Phys. Chem. C* **2009**, *113*, 1242–1250.
14. Tsunoyama, H.; Ichikuni, N.; Sakurai, H.; Tsukuda, T. Effect of Electronic Structures of Au Clusters Stabilized by Poly(*N*-vinyl-2-pyrrolidone) on Aerobic Oxidation Catalysis. *J. Am. Chem. Soc.* **2009**, *131*, 7086–7093.
15. Zhang, G. R.; Xu, B. Q. Surprisingly Strong Effect of Stabilizer on the Properties of Au Nanoparticles and Pt^Au Nanostructures in Electrocatalysis. *Nanoscale* **2010**, *2*, 2798–2804.
16. Du, B.; Zaluzhna, O.; Tong, Y. Y. Electrocatalytic Properties of Au@Pt Nanoparticles: Effects of Pt Shell Packing Density and Au Core Size. *Phys. Chem. Chem. Phys.* **2011**, *13*, 11568–11574.
17. Mohr, C.; Hofmeister, H.; Claus, P. The Influence of Real Structure of Gold Catalysts in the Partial Hydrogenation of Acrolein. *J. Catal.* **2003**, *213*, 86–94.
18. Zhao, D.; Xu, B. Q. Enhancement of Pt Utilization in Electrocatalysts by Using Gold Nanoparticles. *Angew. Chem., Int. Ed.* **2006**, *45*, 4955–4959.
19. Zhao, D.; Xu, B. Q. Platinum Covering of Gold Nanoparticles for Utilization Enhancement of Pt in Electrocatalysts. *Phys. Chem. Chem. Phys.* **2006**, *8*, 5106–5114.
20. Kristian, N.; Yan, Y.; Wang, X. Highly Efficient Submonolayer Pt-Decorated Au Nano-Catalysts for Formic Acid Oxidation. *Chem. Commun.* **2008**, 353–355.
21. Zhao, D.; Wang, Y. H.; Xu, B. Q. Pt Flecks on Colloidal Au (Pt^Au) as Nanostructured Anode Catalysts for Electrooxidation of Formic Acid. *J. Phys. Chem. C* **2009**, *113*, 20903–20911.
22. Roduner, E. Size Matters: Why Nanomaterials Are Different. *Chem. Soc. Rev.* **2006**, *35*, 583–592.
23. van Bokhoven, J. A.; Miller, J. T. d Electron Density and Reactivity of the d Band as a Function of Particle Size in Supported Gold Catalysts. *J. Phys. Chem. C* **2007**, *111*, 9245–9249.
24. Phala, N. S.; van Steen, E. Intrinsic Reactivity of Gold Nanoparticles: Classical, Semi-Empirical and DFT Studies. *Gold Bull.* **2007**, *40*, 150–153.
25. Min, M.; Kim, C.; Yang, Y. I.; Yi, J.; Lee, H. Surface-Specific Overgrowth of Platinum on Shaped Gold Nanocrystals. *Phys. Chem. Chem. Phys.* **2009**, *11*, 9759–9765.
26. Xiong, Y. J.; Wiley, B.; Xia, Y. N. Nanocrystals with Unconventional Shapes—A Class of Promising Catalysts. *Angew. Chem., Int. Ed.* **2007**, *46*, 7157–7159.
27. Capon, A.; Parsons, R. The Oxidation of Formic Acid at Noble Metal Electrodes Part III. Intermediates and Mechanism on Platinum Electrodes. *J. Electroanal. Chem.* **1973**, *45*, 205–231.
28. Lu, G.; Crown, A.; Wieckowski, A. Formic Acid Decomposition on Polycrystalline Platinum and Palladized Platinum Electrodes. *J. Phys. Chem. B* **1999**, *103*, 9700–9711.
29. Lovic, J. D.; Tripkovic, A. V.; Gojkovic, S. L.; Popovic, K. D.; Tripkovic, D. V.; Olszewski, P.; Kowal, A. Kinetic Study of Formic Acid Oxidation on Carbon-Supported Platinum Electrocatalyst. *J. Electroanal. Chem.* **2005**, *581*, 294–302.
30. Park, S.; Xie, Y.; Weaver, M. J. Electrocatalytic Pathways on Carbon-Supported Platinum Nanoparticles: Comparison of Particle-Size-Dependent Rates of Methanol, Formic Acid, and Formaldehyde Electrooxidation. *Langmuir* **2002**, *18*, 5792–5798.
31. Peng, Z.; Yang, H. PtAu Bimetallic Heteronanostructures Made by Post-synthesis Modification of Pt-on-Au Nanoparticles. *Nano Res.* **2009**, *2*, 406–415.
32. Wang, Y. H.; Zhao, D.; Xu, B. Q. Electro-oxidation of Formic Acid on Nanostructured Pt-on-Au (Pt^Au) Electrocatalysts. *Chin. J. Catal.* **2008**, *29*, 297–302.
33. Hammer, B.; Nielsen, O. H.; Nørskov, J. K. Structure Sensitivity in Adsorption: CO Interaction with Stepped and Reconstructed Pt Surfaces. *Catal. Lett.* **1997**, *46*, 31–35.
34. Pedersen, M. O.; Helveg, S.; Ruban, A.; Stensgaard, I.; Laegsgaard, E.; Nørskov, J. K.; Besenbacher, F. How a Gold Substrate Can Increase the Reactivity of a Pt Overlayer. *Surf. Sci.* **1999**, *426*, 395–409.
35. Zhou, W. P.; Lewera, A.; Larsen, R.; Masel, R. I.; Bagus, P. S.; Wieckowski, A. Size Effects in Electronic and Catalytic Properties of Unsupported Palladium Nanoparticles in Electrooxidation of Formic Acid. *J. Phys. Chem. B* **2006**, *110*, 13393–13398.
36. Roudgar, A.; Gross, A. Local Reactivity of Supported Metal Clusters: Pd−N on Au(111). *Surf. Sci.* **2004**, *559*, L180–L186.
37. Stamenkovic, V. R.; Mun, B. S.; Arenz, M.; Mayrhofer, K. J. J.; Lucas, C. A.; Wang, G.; Ross, P. N.; Markovic, N. M. Trends in Electrocatalysis on Extended and Nanoscale Pt−Bimetallic Alloy Surfaces. *Nat. Mater.* **2007**, *6*, 241–247.
38. Stamenkovic, V. R.; Mun, B. S.; Mayrhofer, K. J. J.; Ross, P. N.; Markovic, N. M.; Rossmeisl, J.; Greeley, J.; Nørskov, J. K. Changing the Activity of Electrocatalysts for Oxygen Reduction by Tuning the Surface Electronic Structure. *Angew. Chem., Int. Ed.* **2006**, *45*, 2897–2901.
39. Gong, K. P.; Su, D.; Adzic, R. R. Platinum-Monolayer Shell on $AuNi_{0.5}Fe$ Nanoparticle Core Electrocatalyst with High Activity and Stability for the Oxygen Reduction Reaction. *J. Am. Chem. Soc.* **2010**, *132*, 14364–14366.
40. Trasatti, S.; Petrii, O. A. Real Surface-Area Measurements in Electrochemistry. *Pure Appl. Chem.* **1991**, *63*, 711–734.
41. Adic, R. R.; Markovic, N. M.; Vesovic, V. B. Structural Effects in Electrocatalysis: Oxygen Reduction on the Au (100)

Single Crystal Electrode. *J. Electroanal. Chem.* **1984**, *165*, 105–120.
42. Schmidt, T. J.; Stamenkovic, V.; Arenz, M.; Markovic, N. M.; Ross, P. N. Oxygen Electrocatalysis in Alkaline Electrolyte: Pt(*hkl*), Au(*hkl*) and the Effect of Pd-Modification. *Electrochim. Acta* **2002**, *47*, 3765–3776.
43. Hammer, B.; Nørskov, J. K. Theoretical Surface Science and Catalysis—Calculations and Concepts. *Adv. Catal.* **2000**, *45*, 71–129.
44. Jiang, T.; Mowbray, D. J.; Dobrin, S.; Falsig, H.; Hvolbæk, B.; Bligaard, T.; Nørskov, J. K. Trends in CO Oxidation Rates for Metal Nanoparticles and Close-Packed, Stepped, and Kinked Surfaces. *J. Phys. Chem. C* **2009**, *113*, 10548–10553.
45. Park, I.; Lee, K.; Choi, J.; Park, H.; Sung, Y. Surface Structure of Pt-Modified Au Nanoparticles and Electrocatalytic Activity in Formic Acid Electro-oxidation. *J. Phys. Chem. C* **2007**, *111*, 19126–19133.
46. Obradović, M. D.; Rogan, J. R.; Babić, B. M.; Tripković, A. V.; Gautam, A. R. S.; Radmilović, V. R.; Gojković, S. L. Formic Acid Oxidation on Pt−Au Nanoparticles: Relation between the Catalyst Activity and the Poisoning Rate. *J. Power Sources* **2012**, *197*, 72–79.
47. Ruban, A.; Hammer, B.; Stoltze, P.; Skriver, H. L.; Nørskov, J. K. Surface Electronic Structure and Reactivity of Transition and Noble Metals. *J. Mol. Catal. A: Chem.* **1997**, *115*, 421–429.
48. Hoshi, N.; Kida, K.; Nakamura, M.; Nakada, M.; Osada, K. Structural Effects of Electrochemical Oxidation of Formic Acid on Single Crystal Electrodes of Palladium. *J. Phys. Chem. B* **2006**, *110*, 12480–12484.
49. Ji, X. L.; Lee, K. T.; Holden, R.; Zhang, L.; Zhang, J. J.; Botton, G. A.; Couillard, M.; Nazar, L. F. Nanocrystalline Intermetallics on Mesoporous Carbon for Direct Formic Acid Fuel Cell Anodes. *Nat. Chem.* **2010**, *2*, 286–293.